ADVANCED ENERGY MATERIALS

Supporting Information

for *Adv. Energy Mater.,* DOI: 10.1002/aenm.201601582

Thermal Induced Strain Relaxation of 1D Iron Oxide for Solid Electrolyte Interphase Control and Lithium Storage Improvement

Kangning Zhao, Mingying Wen, Yifan Dong, Lei Zhang, Mengyu Yan, Wangwang Xu, Chaojiang Niu, Liang Zhou, Qiulong Wei, Wenhao Ren, Xuanpeng Wang, and Liqiang Mai**

Supporting Information

Thermal Induced Strain Relaxation for Solid Electrolyte Interphase Control and Lithium Storage Improvement

*Kangning Zhao[§a], Mingying Wen[§a], Yifan Dong[§ab], Lei Zhang[a], Mengyu Yan[a], Wangwang Xu[c], Chaojiang Niu[a], Liang Zhou[*a], Qiulong Wei[a], Wenhao Ren[a], Xuanpeng Wang[a], Liqiang Mai[*a]*

K.N. Zhao[a], M.Y. Wen[a], Y.F. Dong[a], L. Zhang[a], M.Y. Yan[a], W.W. Xu[a], C.J. Niu[a], Prof. L. Zhou[a], Q.L. Wei [a], W.H. Ren[a], X.P. Wang[a], Prof. L. Q. Mai[a]

State Key Laboratory of Advanced Technology for Materials Synthesis and Processing, Wuhan University of Technology

Wuhan 430070, China

Y.F. Dong[b]

Department of Chemistry，University of Wisconsin-Madison, WI 53706, USA.

W.W. Xu[c]

Department of Mechanical and Industrial Engineering, Louisiana State University, Baton Rouge, LA, USA

E-mail: mlq518@whut.edu.cn (L. Q. Mai) ; liangzhou@whut.edu.cn(L. Zhou)

Keywords: Thermal induced strain relaxation; Solid Electrolyte Interphase Control; Template-engaged Reaction; One-dimensional nanostructure; Lithium storage

The calculation of the standard potential.

The half reaction can be described as follows:

$$MnOOH + 3\ H^+ + e^- = Mn^{2+} + 2\ H_2O$$

According to the literature reported (J. D. Hem, C. E. Roberson and R. B. Fournier, *Water Resources Research*, 1982, 18, 563.), the Gibbs Free energy of each component is shown below:

$\Delta G^{\Theta}_{MnOOH}$ = -129.80 kcal/mol $\Delta G^{\Theta}_{Mn^{2+}}$ = -54.50 kcal/mol $\Delta G^{\Theta}_{H_2O}$ = -56.69 kcal/mol

The Gibbs Free energy of the reaction is below:

$$\Delta G^{\Theta}_{Total} = \Delta G^{\Theta}_{Mn^{2+}} + 2\ \Delta G^{\Theta}_{H_2O} - \Delta G^{\Theta}_{MnOOH} = -38.08\ kcal/mol = -159.40\ kJ/mol$$

According to Nernst Equation ($\Delta G^{\Theta}_{Total} = -zF\Delta E^{\Theta}$), the standard potential can be obtained:

$$\Delta E^{\Theta} = \Delta G^{\Theta}_{Total}/(-zF) = 1.65\ V$$

Thus the two half reactions are shown below:

Half reaction 1: $MnOOH + 3\ H^+ + e^- = Mn^{2+} + 2\ H_2O$ $\Delta E^{\Theta} = 1.65$ V

Half reaction 2: $Fe^{3+} + e^- = Fe^{2+}$ $\Delta E^{\Theta} = 0.771$ V

Table S1

	Current Density	2nd Capacity	Cycle number	Capacity fading per cycle(vs. 2nd Capacity)	Rate performance	Reference
Ladder-like Fe_2O_3 nanostructures	5	960	1200	0.027 %	783 mA h g^{-1} at 5 A g^{-1}	This work
Multi-shelled hollow microspheres	0.05	1723	50	0.023 %	1100 mA h g^{-1} at 1 A g^{-1}	1

3D Hierarchical Porous α-Fe_2O_3 Nanosheets	2.012	~750	1000	/(Capacity increase)	705.4 mA h g^{-1} at 4 A g^{-1}	2
Bubble-Nanorod-Structured Fe_2O_3–Carbon Nanofibers	1	968	300	0.054 %	491 mA h g^{-1} at 5 A g^{-1}	3
Fe_3O_4@Fe_3C Core@Shell Nanoparticles	2	624	400	0.0360%	604.8 mA h g^{-1} at 2 A g^{-1}	4
α-Fe_2O_3/HHC	2.014	~810	200	0.160%	550 mA h g^{-1} at 2 A g^{-1}	5
Hollow Fe_2O_3 nanosphere aggregates	3	~1000	100	0.0486%	505 mA h g^{-1} at 10 A g^{-1}	6
Fe_2O_3/GS Aerogels	2	~1200	1000	0.0389%	520 mA h g^{-1} at 4 A g^{-1}	7
Fe_2O_3@CHTS	0.2	1149	70	0.0286%	962 mA h g^{-1} at 0.8 A g^{-1}	8
Fe_2O_3/Fe_3C-graphene heterogeneous thin film	2.61	573	1000	0.0100%	518 mA h g^{-1} at 6.6 A g^{-1}	9
Fe_2O_3@PANI	0.1	958	100	0.0678%	681 mA h g^{-1} at 10 A g^{-1}	10

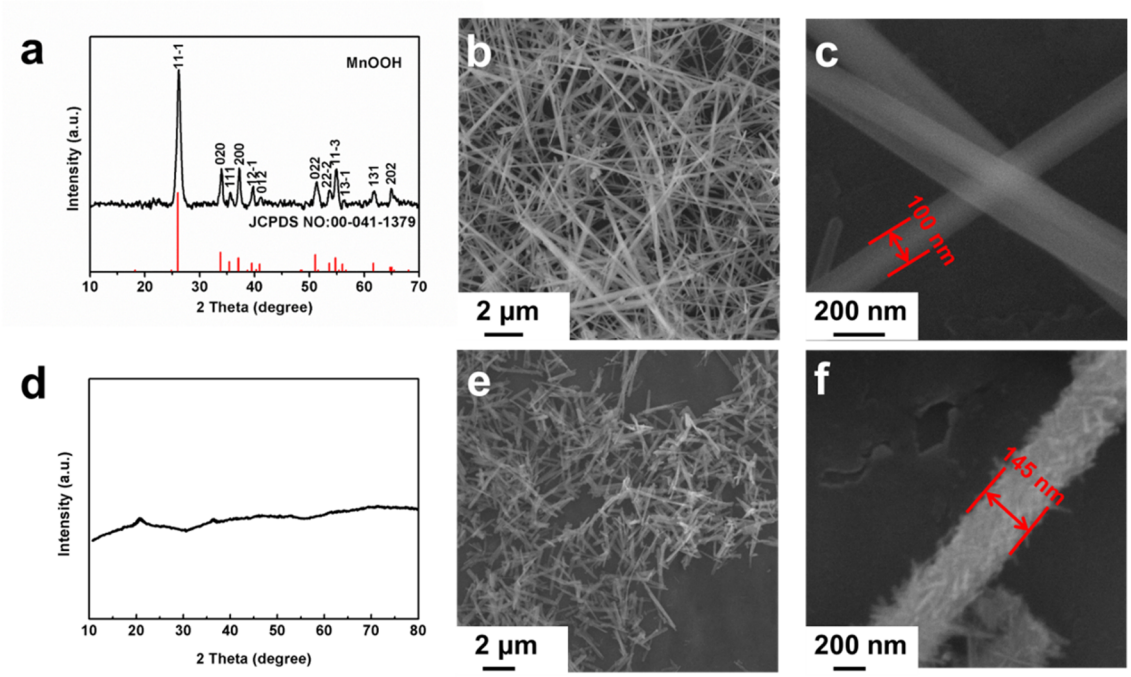

Figure S1. (a) XRD pattern of MnOOH nanowires. (b, c) SEM images of MnOOH nanowires. (d) XRD pattern of $Fe(OH)_3$ nanotubes. (e, f) SEM images of $Fe(OH)_3$ nanotubes.

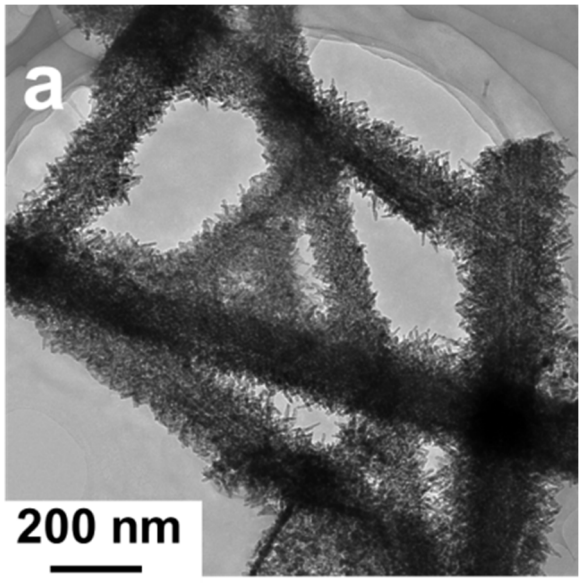

Figure S2. TEM images of $Fe(OH)_3$ nanotubes.

Table S2

Reaction time	Mn/Fe atomic ratio
10 min	13.35:5.25
30 min	1.13:3.81
1 h	0.25:1.92
2 h	0.18:3.07
6 h	0.13:5.61
12 h	0:4.43

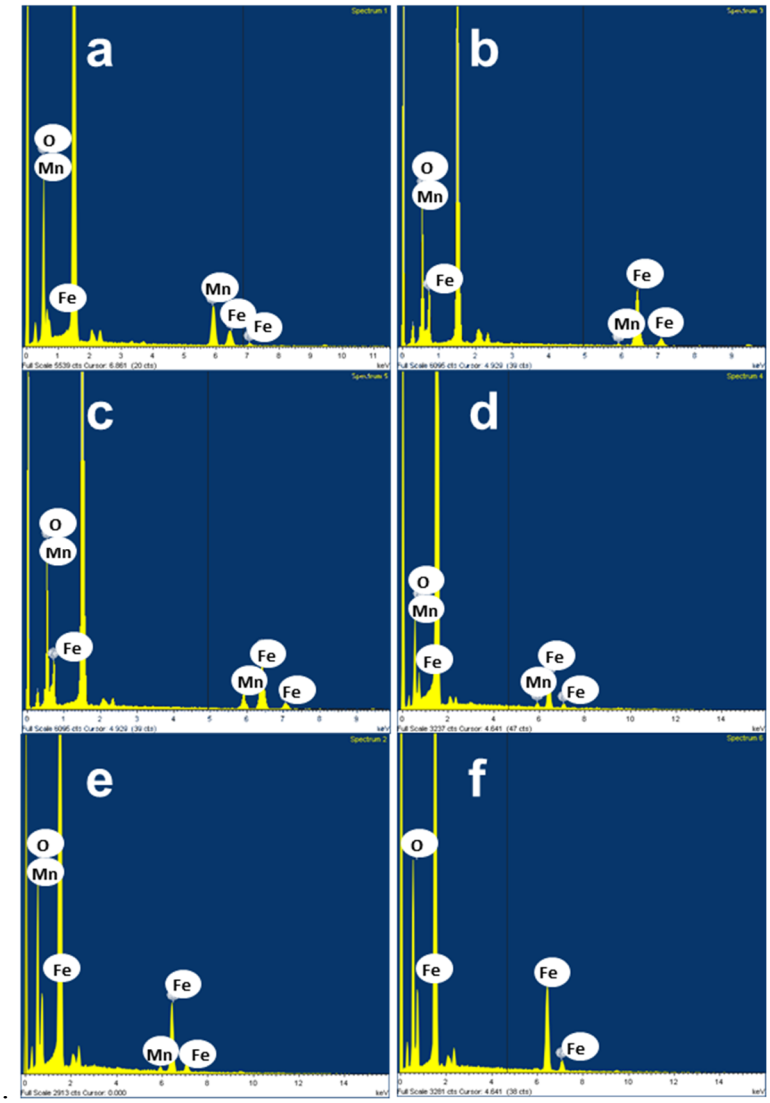

Figure S3. (a-f) EDX spectrum of the products at time of 10 min (a), 30 min (b), 1 h (c), 2 h (d), 6 h (e), and 12 h (f), respectively.

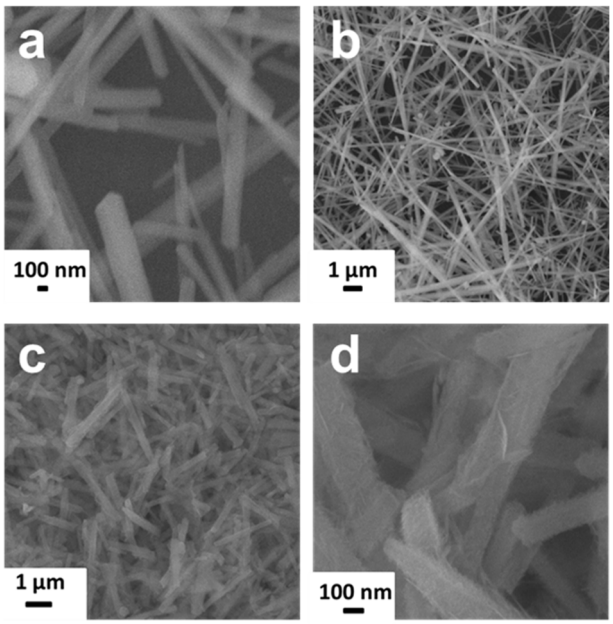

Figure S4. (a, b) SEM images of products in pure alcohol. (c, d) SEM images of products in pure water.

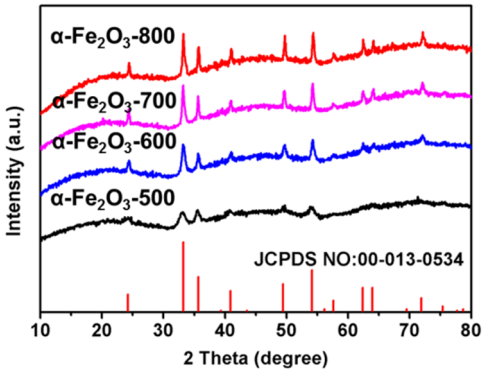

Figure S5. XRD pattern of (a) α-Fe_2O_3-500(hierarchal nanotubes), (b) α-Fe_2O_3-600 (hierarchal nanotubes), (c) α-Fe_2O_3-700(porous nanotubes), and (d) α-Fe_2O_3-800 (laddered nanostructure), respectively.

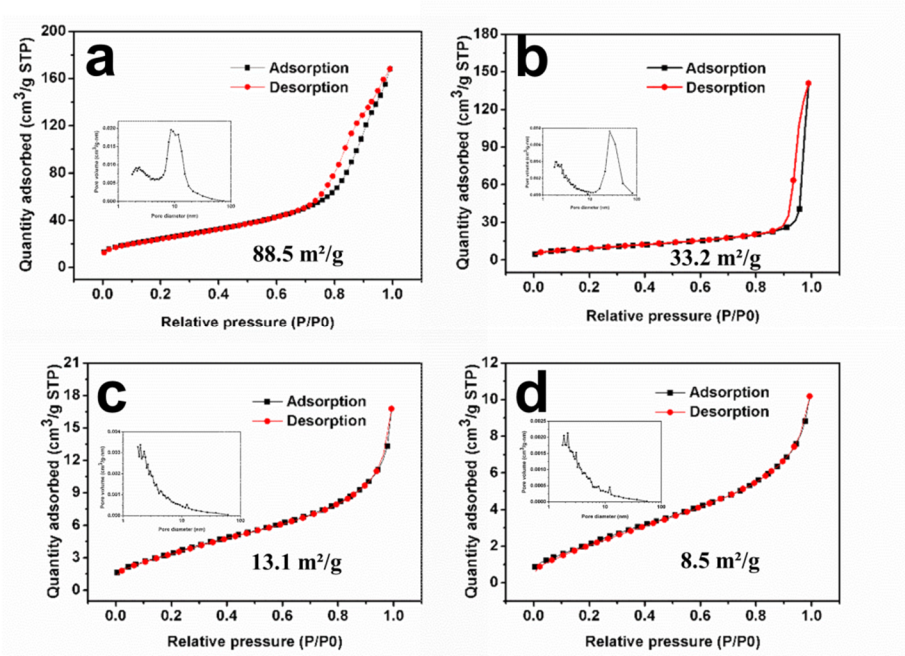

Figure S6. Nitrogen adsorption−desorption isotherms of (a) α-Fe_2O_3-500(hierarchal nanotubes), (b) α-Fe_2O_3-600 (hierarchal nanotubes), (c) α-Fe_2O_3-700(porous nanotubes), and (d) α-Fe_2O_3-800 (laddered nanostructure), respectively.

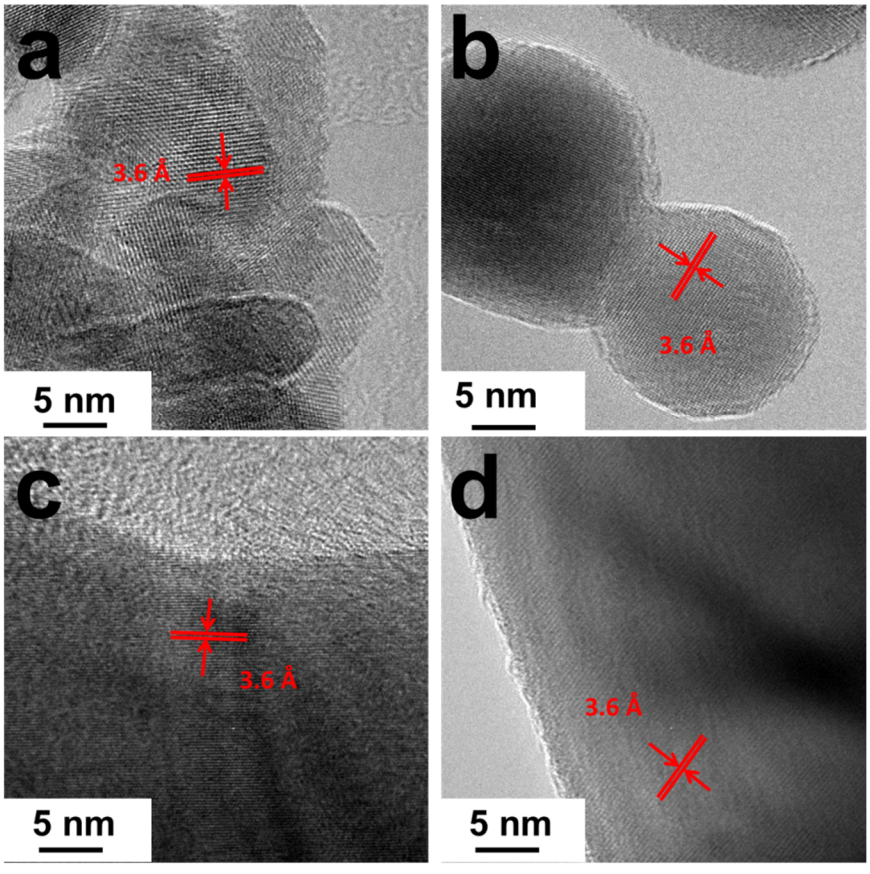

Figure S7. HRTEM images of (a) α-Fe_2O_3-500(hierarchal nanotubes), (b) α-Fe_2O_3-600 (hierarchal nanotubes), (c) α-Fe_2O_3-700(porous nanotubes), and (d) α-Fe_2O_3-800 (laddered nanostructure), respectively.

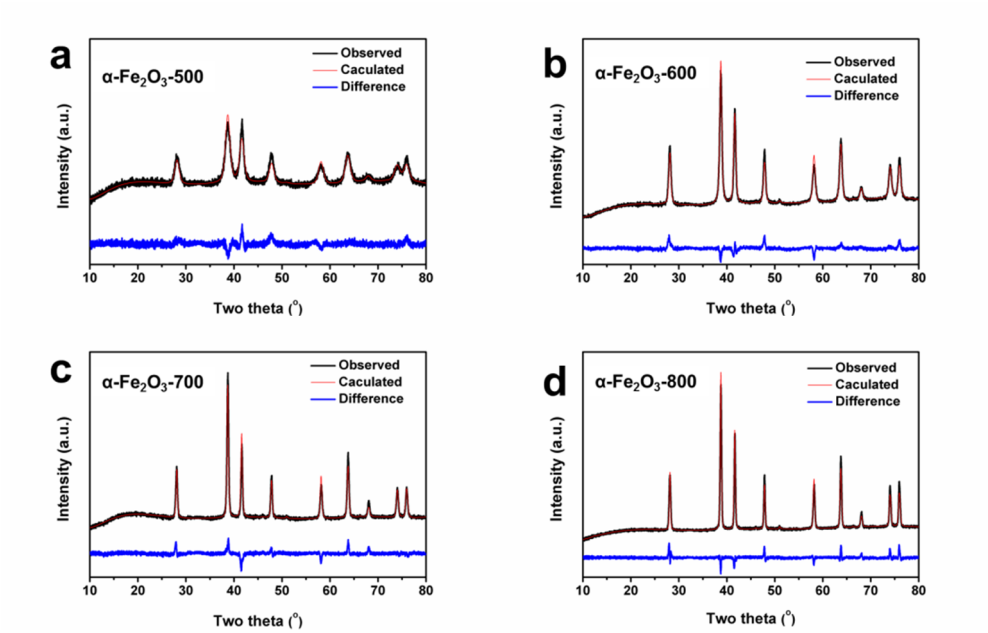

Figure S8. Rietveld refinement XRD pattern of α-Fe_2O_3-500 (hierarchal nanotubes), α-Fe_2O_3-600 (porous hierarchal nanotubes), α-Fe_2O_3-700 (porous nanotubes), and α-Fe_2O_3-800 (laddered nanostructure).

Table S3

	a (Å)	c (Å)	Cell Volume ($Å^3$)	Lvol-FWHM	e_0	Rwp (%)
α-Fe_2O_3-500	5.043(6)	13.778(6)	303.54797	8.745	0.00260	3.363
α-Fe_2O_3-600	5.038(1)	13.756(1)	302.38801	19.490	0.00164	3.136
α-Fe_2O_3-700	5.037(5)	13.741(2)	301.99214	27.168	0.00068	3.808
α-Fe_2O_3-800	5.040(8)	13.755(4)	302.69753	33.962	0.00012	3.884

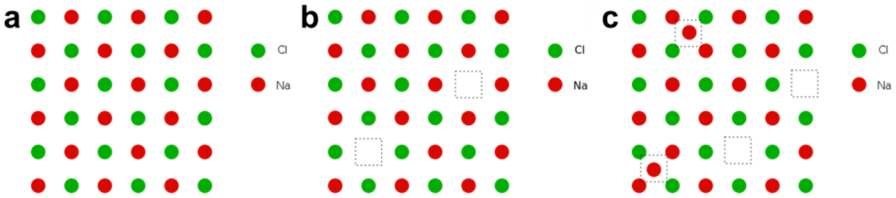

Figure S9. Schematic illustrations of the defect-free NaCl structure (a), Schottky defects within the NaCl structure (b), and two Frenkel defects within the NaCl structure (c).

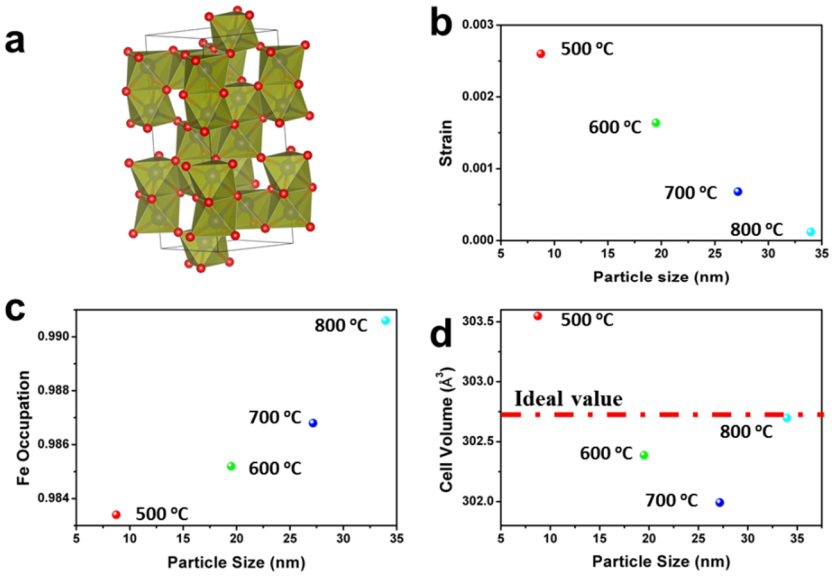

Figure S10. (a) Crystal structure of α-Fe_2O_3. (b) Particle size *vs*. strain. (c) Particle size *vs*. Fe occupation. (d) Particle size *vs*. cell volume.

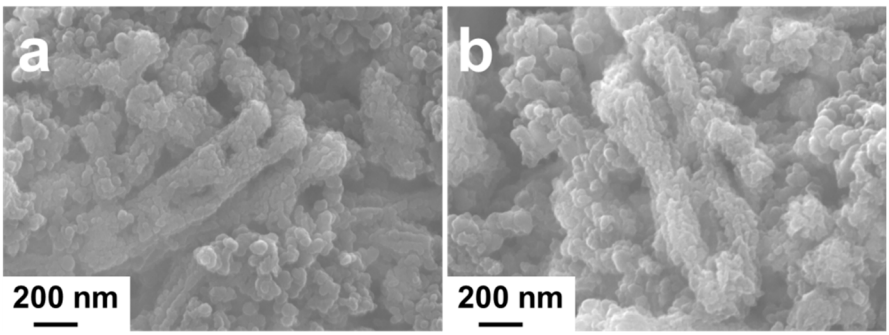

Figure S11. SEM images of α-Fe_2O_3-800 when discharged 0.01 V in the initial cycle.

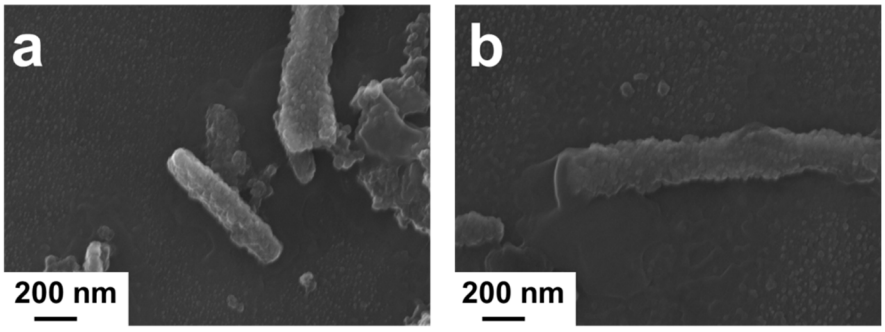

Figure S12. SEM images of α-Fe_2O_3-500 when discharged 0.01 V in the initial cycle.

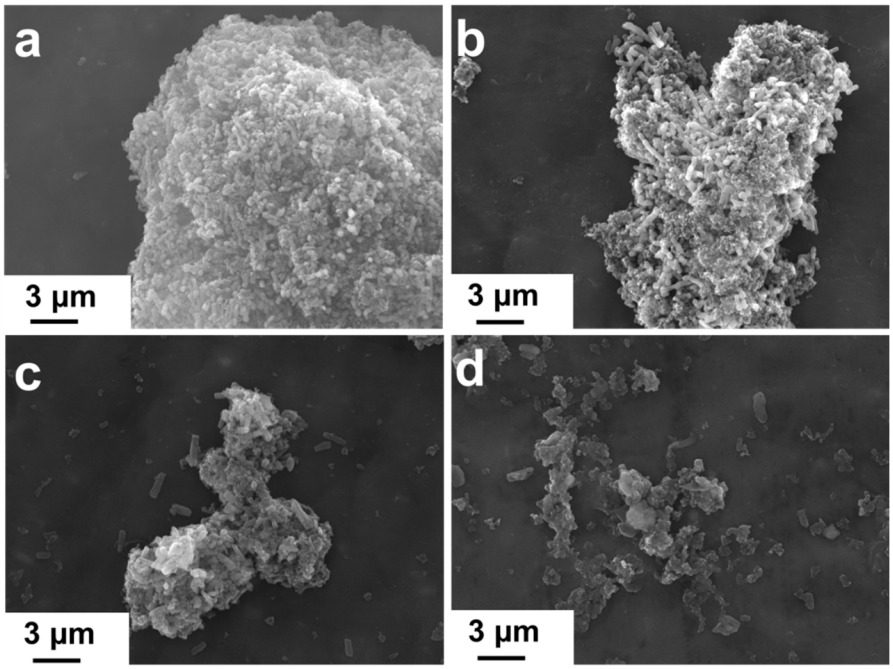

Figure S13. (a, b) SEM images of α-Fe_2O_3-800 after 10 cycles. (c, d) SEM images ofα-Fe_2O_3-500 after 10 cycles.

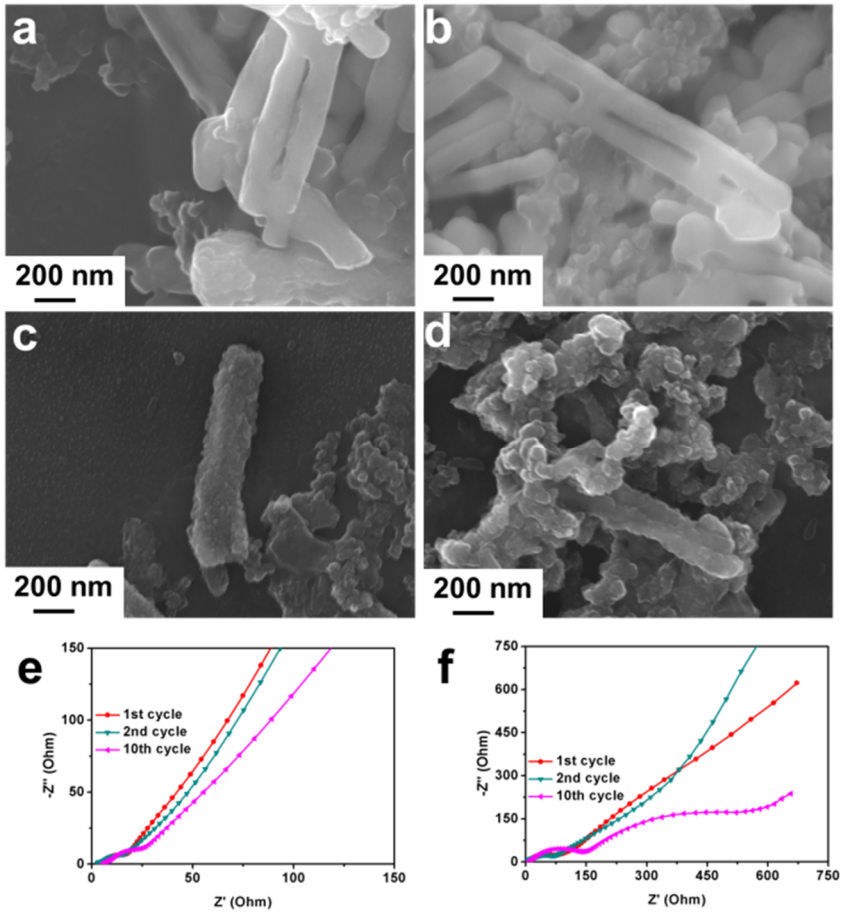

Figure S14. (a) SEM images of α-Fe_2O_3-800 after the first cycle. (b) SEM images of α-Fe_2O_3-800 after ten cycles. (c) SEM images of α-Fe_2O_3-500 after the first cycle. (d) SEM images of α-Fe_2O_3-500 after ten cycles. Insets are magnified SEM images. (e, f) AC impedance response of α-Fe_2O_3-800 and α-Fe_2O_3-500 after first, second, and tenth cycle, respectively

Table S4

	R_1 (Ω)	R_2 (Ω)	R_3 (Ω)
α-Fe_2O_3-800-1st cycle	2.6	2.4	10.5
α-Fe_2O_3-800-2nd cycle	2.9	2.8	10.6
α-Fe_2O_3-800-10th cycle	5.0	4.7	10.4
α-Fe_2O_3-500-1st cycle	2.7	2.5	32.7
α-Fe_2O_3-500-2nd cycle	2.9	2.8	47.7
α-Fe_2O_3-500-10th cycle	5.6	113.5	184.3

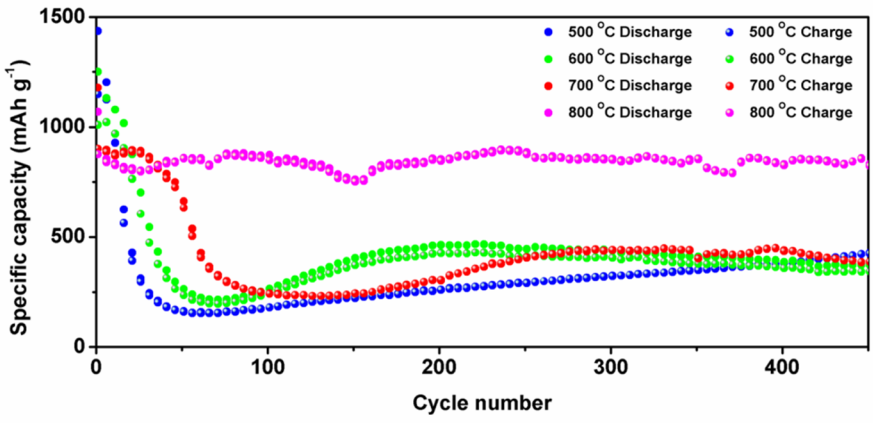

Figure S15. Cycling performances of α-Fe_2O_3-500 (hierarchal nanotubes), α-Fe_2O_3-600 (hierarchal nanotubes), α-Fe_2O_3-700 (porous nanotubes), and α-Fe_2O_3-800 (laddered nanostructure) at 2 A g^{-1}.

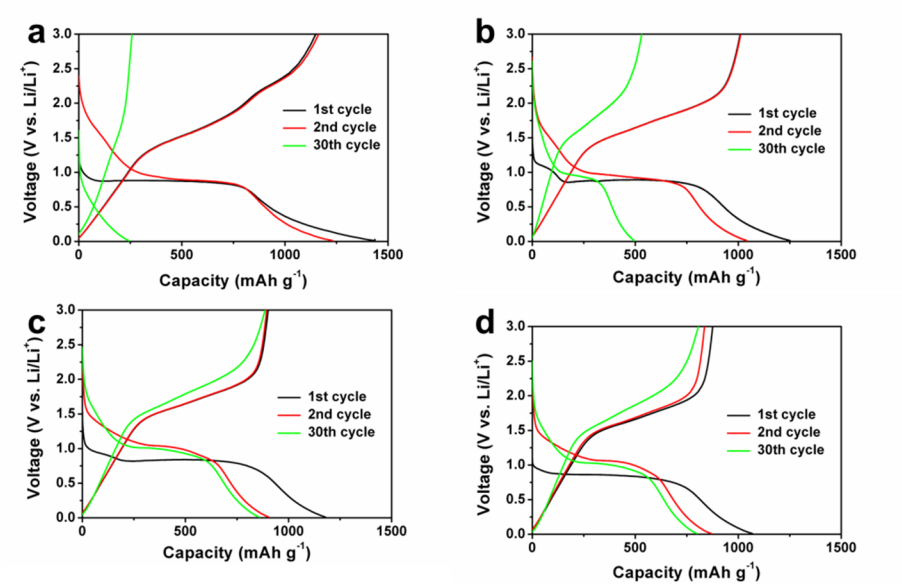

Figure S16. Charge-discharge curves of (a) α-Fe_2O_3-500 (hierarchal nanotubes), (b) α-Fe_2O_3-600 (porous hierarchal nanotubes), (c) α-Fe_2O_3-700 (porous nanotubes), and (d) α-Fe_2O_3-800 (laddered nanostructure) at 2 A g^{-1}.

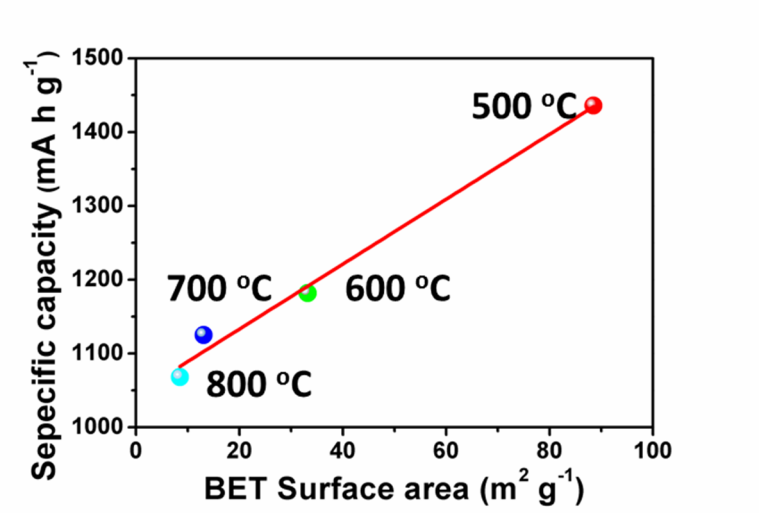

Figure S17. the surface area vs. intial discharge capacity.

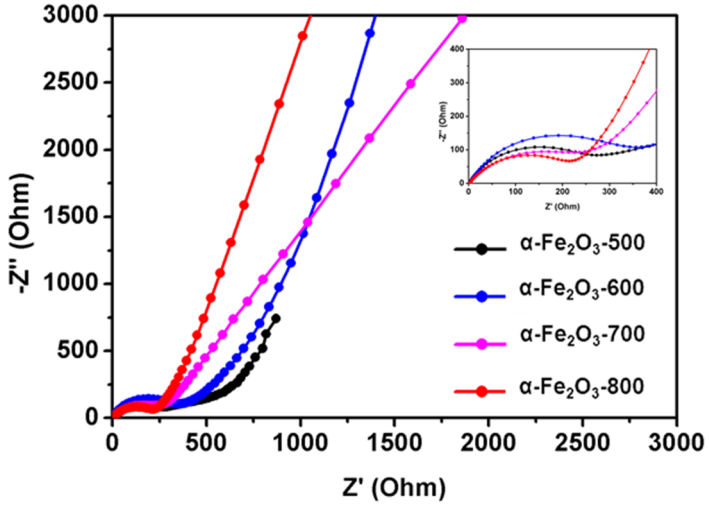

Figure S18. AC impedance responses of α-Fe_2O_3-500 (hierarchal nanotubes), α-Fe_2O_3-600 (porous hierarchal nanotubes), α-Fe_2O_3-700 (porous nanotubes), and α-Fe_2O_3-800 (laddered nanostructure) at OCP.

1. S. M. Xu, C. M. Hessel, H. Ren, R. B. Yu , Q. Jin, M. Yang, H. J. Zhao, D. Wang, α-Fe_2O_3 multi-shelled hollow microspheres for lithium ion battery anodes with superior capacity and charge retention, Energy Environ. Sci., 2014, 7, 632-637
2. Cao K, Jiao L, Liu H, et al. 3D Hierarchical Porous α-Fe_2O_3 Nanosheets for High-Performance Lithium-Ion Batteries[J]. Advanced Energy Materials, 2015, 5(4).
3. Cho J S, Hong Y J, Kang Y C. Design and Synthesis of Bubble-Nanorod-Structured Fe_2O_3–Carbon Nanofibers as Advanced Anode Material for Li-Ion Batteries[J]. ACS nano, 2015, 9(4): 4026-4035.
4. Beyond Yolk–Shell Nanoparticles: Fe_3O_4@Fe_3C Core@Shell Nanoparticles as Yolks and Carbon Nanospindles as Shells for Efficient Lithium Ion Storage, ACS Nano, 2015, 9 (3), pp 3369–3376
5. Dong H, Zhang H, Xu Y, et al. Facile synthesis of α-Fe_2O_3 nanoparticles on porous human hair-derived carbon as improved anode materials for lithium ion batteries[J]. Journal of Power Sources, 2015, 300: 104-111.

6. Jung Sang Cho , Young Jun Hong , Jong-Heun Lee and Yun Chan Kang, Design and synthesis of micron-sized spherical aggregates composed of hollow Fe_2O_3 nanospheres for use in lithium-ion batteries, Nanoscale, 2015, 7, 8361-8367
7. Wang R, Xu C, Du M, et al. Solvothermal-Induced Self-Assembly of Fe_2O_3/GS Aerogels for High Li-Storage and Excellent Stability[J]. Small, 2014, 10(11): 2260-2269.
8. Gao G, Yu L, Wu H B. Hierarchical Tubular Structures Constructed by Carbon-coated α-Fe_2O_3 Nanorods for Highly Reversible Lithium Storage[J]. Small, 2014, 10(9): 1741-1745.
9. Yang Y, Fan X, Casillas G, et al. Three-dimensional nanoporous Fe_2O_3/Fe_3C-graphene heterogeneous thin films for lithium-ion batteries[J]. ACS nano, 2014, 8(4): 3939-3946.
10. Jeong J M, Choi B G, Lee S C, et al. Hierarchical hollow spheres of Fe_2O_3@ polyaniline for lithium ion battery anodes[J]. Advanced Materials, 2013, 25(43): 6250-6255.